Lawrence Berkeley National Laboratory

Title
Laser-Generated Ag Nanoparticles in Mesoporous TiO2 Films: Formation Processes and Modeling-Based Size Prediction

Authors
Ma, Hongfeng
Bakhti, Said
Rudenko, Anton
et al.

An interplay between thermal growth and photo-oxidation of laser-irradiated Ag nanoparticles in TiO$_2$ matrix

Hongfeng Ma,[†] Said Bakhti,[‡] Anton Rudenko,[†] Francis Vocanson,[†] Daniel S. Slaughter,[‡] Nathalie Destouches,[*,†] and Tatiana E. Itina[*,†,¶]

†*Laboratoire Hubert Curien, UMR CNRS 5516/UJM/Université de Lyon, 18 Rue Pr. Lauras, 42000 Saint-Etienne, France*

‡*Chemical Sciences, Lawrence Berkeley National Laboratory, Berkeley, CA 94720, USA*

¶*ITMO University, 49 Kronverksky pr., 197101 Saint-Petersburg, Russia*

E-mail: nathalie.destouches@univ-st-etienne.fr; tatiana.itina@univ-st-etienne.fr

Phone: +33 (0)4 77 91 57 80. Fax: +33 (0)4 77 91 57 81

Abstract

Nanoparticle growth is induced in TiO_2 films impregnated by Ag ions by scanning continuous wave laser irradiation. This self-consistent process is accompanied by size-related absorption and temperature-dependent diffusion. Based on both numerical and experimental studies, nanoparticle growth is investigated demonstrating how a combination of thermally activated nanoparticle growth with photo-oxidation, determine film temperature and optical properties. The obtained results not only explain several experimental findings, but also provide new insights into the nanoparticle growth mechanisms thus extending potential applications to many promising fields involving plasmonic nanocomposite materials, such as photonics, color printing, catalysis and sensors.

Introduction

Plasmonic nanoparticles (NPs) and nanostructures have great potential in photovoltaics,[1,2] nano-imaging,[3] bio-sensing,[4] photoelectric sensors[5,6] and light engineering metamaterials.[7–9] A lot of plasmonic metasurfaces have been created during the last decade to design new optical functionalities. Most of them resulted from perfectly arranged metallic oligomers and were produced by focused ion beam and electron beam lithography, two techniques that are still expensive, time consuming and not well suited to large surfaces. Nanoimprint lithography of metallic nanostructures overcomes these limitations and is expected to become a way to spread the use of plasmonic metasurfaces at the industrial level. This technique is, however, limited to reproduction of masks. Laser direct writing is another technology that provides more flexibility, is well suited for large scale processing and allows a control of plasmonic properties at sub-wavelength level.

Among the metasurfaces that have great promises for applications is titanium dioxide (TiO_2) loaded with metallic NPs. TiO_2 is one of the most studied and widely applied host-materials due to its unique characteristics, such as excellent optical transmittance in visible

wavelength, high refractive index, and stable chemical properties.[6,10] Additionally, TiO_2 is a good n-type semiconductor material and it allows fast electron acceptance because of the high density of states in the conduction band.[6] However, only ultraviolet light can activate the photovoltaic process due to the intrinsic wide-gap limitations of TiO_2. Embedding silver NPs in such a material forms a Schottky barrier, which boosts the photovoltaic efficiency in the visible region. The plasmonic resonance induces a high density of free electrons whose energies exceed the Schottky barrier and makes an increase in the quantum efficiency possible. This so-called "plasmonic hot-carrier" phenomenon has attracted wide interest in research communities during the past decade.[5,6] By injecting hot-electrons from silver NPs to the surrounding semiconductor matrix, NPs become unstable and tend to dissolve into Ag^+ ions, a mechanism also named photo-oxidation.[11] In the meantime, hot electrons also relax through electron-phonon coupling heating the Ag NPs. This heating leads to other mechanisms, such as chemical reduction of silver ions and NP growth, mechanisms that compete with the aforementioned photo-oxidation tending to shrink the NPs.[12–14]

Using scanning laser writing for such TiO_2:Ag film provides an elegant way of controlling the NP size, organization and anisotropy, and thus to control over the optical properties of such plasmonic metasurfaces. Previously the growth of Ag NPs in mesoporous films of amorphous TiO_2 was investigated as a function of scanning speed for different laser powers and focusing. The first developed model was able to simulate the experimentally observed phenomenon showing that NPs grow only above a speed threshold and tend to oxidize below this threshold.[12] In this model, a set of differential equations was solved numerically to demonstrate the competition between shrinkage and growth during laser writing. Later, the model was improved to simulate the size distribution of the grown NPs as a function of time and speed.[14] These previous numerical studies suffered, however, from several limitations. Namely, they modeled the evolution of the system in a point without considering the effect of heating by the NPs grown few micrometers apart and still under the laser beam. The temperature was then calculated by assuming a homogeneous spatial size distribution of NPs

under the laser spot. This led to a good description of the final NP size distributions as a function of speed, but also to a rather questionable growth kinetics and temperature history.

Here, we propose a two-dimensional (2D) model, which accounts for both thermal and spatial size distribution during laser writing to better investigate the growth kinetics during the laser writing and examine the relative role of the underlying physico-chemical mechanisms involved in the laser-induced nanoparticle size evolution. The Galerkin method and adaptive time stepping techniques are used to solve the nonlinear diffusion-controlled growth model based on the open-source finite element method library (Deal.II 8.5.0).[15] A set of 2D simulations is carried out and compared to new experimental results obtained based on the in-situ transmission measurements. The modeling part summarizes the major physico-chemical processes involved and presents how the thermal equation is coupled. The last part analyzes the obtained results and provides new insights into the dynamics of the system under continuous wave laser scanning. In particular, we examine the importance and interplay of the different mechanisms involved.

Experimental

Sample preparation and in-situ characterization setup

Mesoporous films of amorphous TiO_2 are prepared according to the previously published procedure based on a sol-gel process.[16] The obtained films have pore sizes from 5 to 20 nm and a thickness estimated to be 230±50nm by scanning electron microscopy (SEM - FEI Nova nanoSEM 200) on the cross-section. Silver is introduced in the pores by soaking the mesoporous sample into an ammoniacal silver nitrate solution and small silver nanoparticles are created in the film by exposing it to UV light (400 μWcm^{-2} at 254 nm wavelength). Ag NPs are observed after this process with an averaged size around 3nm.[17] The detailed descriptions of the process were reported previously.[12,16,18–20]

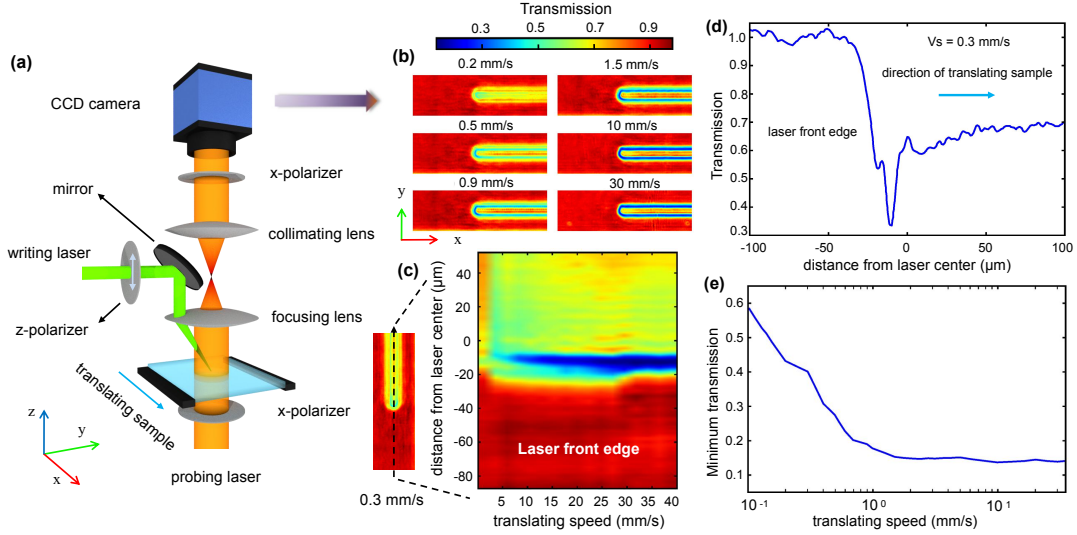Figure 1(a) shows the setup used for in situ measurements of the sample transmission

Figure 1: In-situ transmission experiments. Schematic of the laser setup (a), transmission images of the sample under writing at various translating speeds (b), map showing the transmission along a line parallel to the scanning direction and passing through the beam center (dashed line in the left-handed image) (c), transmission profile along the dashed line of (c) at 0.3 mm/s (d), and the minimum value of transmission along the scanning direction versus scanning speed (e).

during laser writing. The writing laser is a 1W continuous-wave laser emitting at 532 nm and linearly polarized along the y-direction on the sample plane. It is focused on the sample surface by a 5 cm focal length lens. Imaging is performed thanks to a probe nanosecond laser emitting at 527 nm, a wavelength absorbed by growing Ag NPs. The latter is collimated on the sample and then imaged on a CCD camera through a couple of lenses, the first one being the same as the one used to focus the writing beam. Without writing beam, the sample transmittance is fully stable over time, meaning that the nanosecond laser does not modify the nanocomposite film. The imaging beam is linearly polarized (x-axis) with a polarization perpendicular to the writing beam. A linear polarizer just before the camera and a band-pass filter stop all photons from the writing beam before the camera. The writing beam is thus not seen directly on the images where only the transmission changes of the samples are observed. The writing beam position on the images is determined before carrying out in situ experiments. During the experiments, the sample is translated at a constant speed along the x-axis, in the positive direction (according to the sketch in Figure 1(a)).

5

Results

Transmission images are calculated by normalizing the raw images by the averaged intensity recorded in the laser front area. Images are recorded for various scanning speeds (0.1-40 mm/s) and a selection is shown in Figure 1(b). In all cases, transmission varies in the laser written line and our attention is focused on the area located around the laser beam corresponding to the distance "0" in Figure 1(d). The profiles along the line center show the evolution of transmission from a position 100 μm in front of the laser beam center to a position 100 μm after the beam center. The measured transmission strongly decreases in the front (leading) edge of the laser beam before increasing back near the beam center and reaching a constant value in the back edge, as shown in Figure 1(c) and (d). Unexpectedly, the lowest transmission is before the laser center. Moreover, the value decreases with speed until saturation (Figure 1(e)). The transmission inhomogeneity indicates the variation of the NPs' characteristics (such as size, density, shape and order) along the translation direction. To better understand the mechanisms involved in the NP growth and their kinetics during the laser scan, we perform numerical simulations of the measured behaviors accounting for photo-oxidation, thermal diffusion, diffusion-limited growth, reduction, and light scattering.

Modeling

Photo-oxidation

This mechanism is the one that leads to electron emission from NPs upon photon absorption. As sketched in Figure 2(a), when Ag NPs are in contact with TiO2, the electron energy required to allow electrons to leave the NPs is lowered to the value of the Schottky barrier that is created at the interface between the metal and the n-type semiconductor. Electrons excited through the localized surface plasmon resonance of NPs at the laser wavelength (2.4 eV) can cross the Schottky barrier by injection or tunneling. The band bending prevents

the injected electrons from escaping back to the metallic crystals. As a result, the positively charged NPs are unstable and tend to dissolve into Ag^+ ions to keep the neutral state (Figure 2(b)).[12] The number of silver atoms leaving a nanoparticle per unit time due to the above processes was calculated as:[12]

$$n_{oxi}(t) = \eta_0 \frac{\sigma_{abs}(R, \lambda)I(x, y, z, t)}{h\nu} \tag{1}$$

where η_0 is the ionization efficiency, σ_{abs} the absorption cross-section of a nanoparticle of radius R at laser wavelength λ, I the laser intensity, h the Planck constant and ν the light frequency. The ionization efficiency was estimated experimentally in reference.[12] σ_{abs} is calculated by using the classical Mie theory.
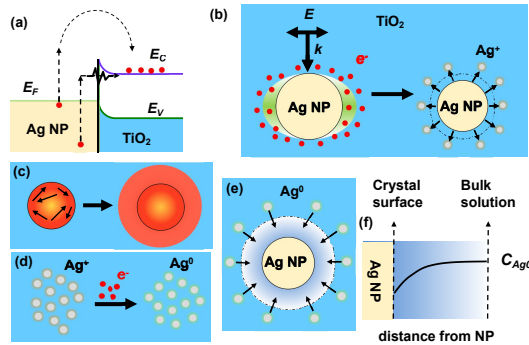

Figure 2: Illustration of the mechanisms involved during the laser excitation of Ag NPs inside the TiO$_2$. Injection and tunneling of plasmon-induced hot-electrons (a), process of photo-oxidation (b), heating (c), reduction (d), and diffusion-limited growth (e) and (f).

Reduction

Figure 2(d) depicts the reduction process where Ag^+ ions can diffuse and recombine with electrons from TiO$_2$ conduction band or from compunds absorbed in the film mesopority such as H$_2$, CO from the atmosphere or NO$_3^-$ from the initial silver nitrate solution.[6,21–24] Silver ions can come from the initial non-reduced silver species present in the film or from the photo-oxidation process. The reduction process leads to Ag^0 monomers that can contribute to the NP growth according to the next mechanism. We assume a homogeneous Ag^+ ion and

Ag^0 monomer distribution for a small cuboid, in which matter conservation is presumed. The decrease of Ag^+ concentration due to the reduction per unit time has the following form: [12,25]

$$\frac{dC_{Ag^+}}{dt}\Big|_{red} = \exp\left(-\frac{E_p}{N_A k_B T}\right) \cdot D_0^{red} \exp\left(-\frac{E_D}{N_A k_B T}\right) \cdot C_{red} C_{Ag^+}^{2/3} \tag{2}$$

where E_p and E_D are the activation energies, D_0^{red} is the diffusion coefficient of the reducer at infinite temperature, C_{red} the concentration of reducing agent, and C_{Ag^+} the concentration of Ag^+. N_A is the Avogadro constant, k_B the Boltzman constant and T the absolute temperature. The first exponential function describes the probability of reduction, while the second term stands for the temperature dependent diffusion of the reducing agents.

Diffusion-controlled growth

Based on previous experiments [12,16,18–20] we suppose that primary tiny NPs, nanoclusters, or "monomers" are formed in the porous matrix due to ultraviolet illumination. A uniform distribution of small and monodisperse NPs is considered in the initial state. Thermal diffusion is considered to be the main initiator of the Ag NP growth in the TiO_2 matrix under laser irradiation (Figure 2(e) and (f)), as was shown by Liu et al. [12,26]

To determine the total number of monomers absorbed by an Ag NP of radius R per unit time, the Fick's first law is applied:

$$n_{abs}(t) = 4\pi R^2 D_{Ag^0}(T) \frac{dC_{Ag^0}}{dr}\Big|_{r=R} \tag{3}$$

where the diffusion coefficient $D_{Ag^0}(T)$ is described by the Arrhenius law as follows: [27,28]

$$D_{Ag^0}(T) = D_{0Ag^0} \exp\left(-\frac{E_{Ag^0}}{N_A k_B T}\right) \tag{4}$$

The homogeneous distribution $C_{Ag^0}(r)$ is calculated by solving the steady state diffusion equation: [29]

$$\frac{1}{r}\frac{\partial^2}{\partial r^2}rC_{Ag^0}(r) = 0 \tag{5}$$

with boundary conditions $C_{Ag^0}(r \rightarrow \infty) = C_{Ag^0}(\infty)$ and $C_{Ag^0}(r = R) = C_{Ag^0}(R)$. The analytic solution is obvious:

$$C_{Ag^0}(r) = C_{Ag^0}(\infty) - [C_{Ag^0}(\infty) - C_{Ag^0}(R)]\frac{R}{r} \tag{6}$$

The equilibrium concentration at the surface of the NP is defined by the following thermodynamic equation:[12,25,29–31]

$$C_{Ag^0}(R) = S_{Ag^0}(1 + \frac{2\gamma\omega}{Rk_BT}) \tag{7}$$

where, S_{Ag^0} is the Ag^0 solubility in mesoporous TiO_2 film, γ the nanoparticle-matrix interfacial tension, and ω the atomic volume of Ag in crystal.

Substituting Eq. 6 and Eq. 7 into Eq. 3, the total amount of monomers absorbed by the Ag NP per unit time is given by:

$$n_{abs}(t) = 4\pi R D_{Ag^0}(T)[C_{Ag^0}^{BS} - S_{Ag^0}(1 + \frac{2\gamma\omega}{Rk_BT})] \tag{8}$$

where E_{Ag^0} the activation energy of diffusion, and $C_{Ag^0}^{BS} \equiv C_{Ag^0}(\infty)$ is the concentration of neutral silver monomers in the matrix.

Heating

In addition to re-radiation and injection, the rest of the absorbed laser energy decays via the electron-phonon and phonon-phonon interactions that heat the irradiated region (Figure 2(c)). The electron relaxations and electron-phonon coupling occur on the time scale of few picoseconds, while phonon-phonon interactions take up to a few nanoseconds.[32–35] Since Ag NPs grow more slowly than the electron-phonon interaction speed, the classical thermal

9

diffusion equation is introduced:

$$C_m \frac{\partial T}{\partial t} = \nabla \cdot (k_m \nabla T) + \alpha_{abs} \cdot I(x, y, z, t) \tag{9}$$

where k_m is the heat conductivity, and C_m the volumetric heat capacity.

Although the absorbed laser energy by a Ag NP is partially relaxed via injection or tunneling, the majority of the energy is finally converted into heat.[5,6,24] It is reasonable to estimate the heating source by taking into account the total absorbed energy. Normally, a laser beam attenuates exponentially in a composite having the mixture of nano-inclusions. Many efforts[36–38] have been devoted to effective medium theories (EMTs) aiming to bridge the Fresnel medium together. Their key common ideas are that, as the concentration of inclusions goes to zero, the effective dielectric function should behave asymptotically as the host medium, and follow the Kramers-Kronig relation.[36] In such media, the Beer-Lambert law describes both light absorption and transmission. Herein, the laser intensity at any position is given by:

$$I(x, y, z, t) = [1 - \Lambda(x, y)]I_0(x, y, t) \exp(-z\alpha_{abs}) \tag{10}$$

where $\alpha_{abs} = \sigma_{abs} \cdot C_{NP}$ is the absorption coefficient, $\Lambda(x, y)$ the surface reflection, and $I_0(x, y, t) = \frac{P_0}{\pi w_0^2 / 2} \cdot \exp\{-\frac{2[(x - V_s t)^2 + y^2]}{w_0^2}\}$ the Gaussian shape laser intensity at time t and point (x, y), where x is the coordinate along the translation direction on the top surface of the TiO$_2$ film. Here, C_{NP} is the NP concentration, w_0 the beam radius at $1/e^2$, P_0 the laser power, and V_s the laser scanning speed.

For simplicity, we use the Maxwell-Garnett (MG) theory to estimate the effective index of the thin film. The surface reflection $\Lambda(x, y)$ is then estimated using the Fresnel equation.

The coupled equations

A link between NP concentration C_{NP} and radius R was previously revealed[12] by analysis of *post mortem* HAADF-STEM micrographs of samples produced at differnt speeds. The dependency is obtained by fitting the experiments according to an empirical law. It is given as follows:

$$C_{NP} = \frac{1}{(a_1 R + a_2)^3} \tag{11}$$

where $a_1 \approx 2.6$ and $a_2 \approx 8.7$nm. The amount of crystallized silver changes in two ways: the variation of size and of the total number of NPs in the volume. Therefore, the differential of concentration is:

$$\frac{dC_{Ag_{cst}}}{dt} = N_{Ag_{cst}} \frac{dC_{NP}}{dt} + C_{NP}[n_{abs}(t) - n_{oxi}(t)] \tag{12}$$

where $N_{Ag_{cst}} = 4\pi R^3/3\omega$ is the number of crystallized Ag atoms in a nanoparticle. For each nanoparticle, the variation of total number of atoms is due to growth and oxidation. Therefore, the radius of a nanoparticle changes as:

$$\frac{dR}{dt} = [n_{abs}(t) - n_{oxi}(t)] \cdot \frac{\omega}{4\pi R^2} \tag{13}$$

Thus, the amount of crystallized Ag atoms in the studied unit cell varies due to the changes of NP concentration as:

$$\begin{aligned} N_{Ag_{cst}} \frac{dC_{NP}}{dt} &= N_{Ag_{cst}} \frac{dC_{NP}}{dR} \frac{dR}{dt} \\ &= \frac{R}{3}[n_{abs}(t) - n_{oxi}(t)] \frac{dC_{NP}}{dR} \end{aligned} \tag{14}$$

where, C_{NP} is the concentration of NPs in the unit cell. The right part of Eq. 14 implies its contribution to oxidation. The mass conservation of Ag in an unit cell leads to the following equations:

$$\frac{dC_{Ag^+}}{dt} = n_{oxi}(t)[C_{NP}(t) + \frac{R(t)}{3}\frac{dC_{NP}}{dR}] - \frac{dC_{Ag^+}}{dt}|_{red} \quad (15)$$

$$\frac{dC_{Ag^0}^{BS}}{dt} = -n_{abs}(t)[C_{NP}(t) + \frac{R(t)}{3}\frac{dC_{NP}}{dR}] + \frac{dC_{Ag^+}}{dt}|_{red} \quad (16)$$

The extended 2D model

Eq. 13 to Eq. 16 describe the full coupled optical, thermal, photo-oxidizing and growing field. The Arrhenius description of diffusion coefficients implies a nonlinear system that makes the 3D calculation extremely time-consuming.

The extended 2D model provides an appropriate approach with less computational efforts to simulate the multi-scale problem and access the spatial information of NP size and temperature in a sample. We simulate the process in cross-section, which consists of two coupled steps. In the first step, the temperature field is computed by FEM. With the knowledge of the heat distribution, the growth, oxidation, and reduction are calculated adaptively by using the Bulirsch-Stoer algorithm.[39] The approach provides second-order accuracy with comparatively few calculation steps. The forecasting time step at each grid is obtained by the Bulirsch-Stoer algorithm. The minimum time step is used for the calculation of temperature and growth in the next step. In this way, few computational efforts are required and the accuracy is guaranteed. The studied structure consists of a TiO_2 film 200nm thick on top of a glass (Figure 3(a)). The effective refractive index of the mesoporous titania film is estimated to $n = 1.7$ and the initial diameter of Ag NPs homogeneously distributed in the film is assumed to be 3 nm.[12] The width of the structure is set to $200\mu m$ and the laser scans the sample from $x = -50\mu m$ to $x = 50\mu m$ to avoid the boundary absorption of heat (Figure 3(b)). Figure 3 shows the simulated results on the top surface (as illustrated in Figure 3 (c)) of the TiO_2 film at a laser writing speed of 50 μm/s. Table S1 (see supplemental material) summarizes the parameters used in simulations.

Results and discussions

The 2D model clearly demonstrates the spatial inhomogeneity during the kinetic process. For instance, as one can see in Figure 3(d), the NP's spatial-size-distribution (SSD) varies from uniform (3 nm in diameter) at the initial stage to non-uniform upon laser writing with big NPs formed at the beginning of the line (43 nm) and under the laser beam (20 nm), whereas the final NP size at the middle of the laser line is 6.8 nm after laser irradiation. Simultaneously, the temperature profile (Figure 3(e)) changes with its maximum value rapidly increasing to 870 °C at the beginning and more slowly decreasing to the steady one at 528 °C after translating the sample by about 25 μm. Figure 3(f) shows the laser profiles during the writing.
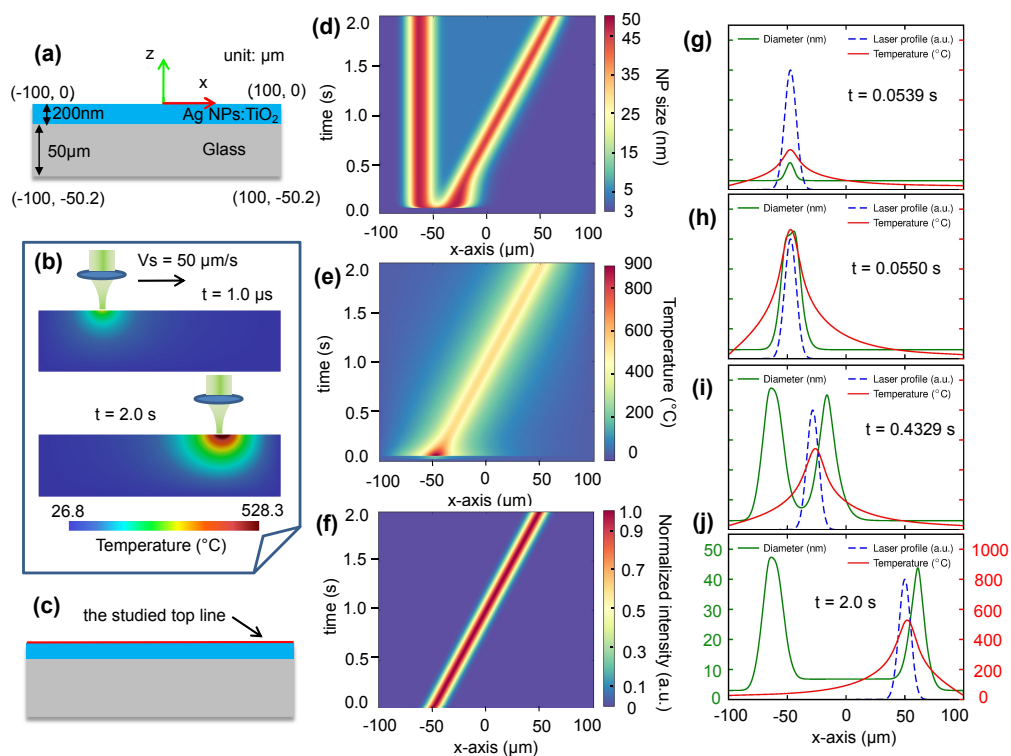

Figure 3: Simulations of the extended 2D model. The structure used in calculations (a), and an example of the temperature distributions at different times (b). Time variation maps of NPs size (d), temperature (e), normalized light intensity (f) along the translation diretion of the lase beam at the top surface (c) of the film. (g), (h), (i) and (j) stand for the different states of the sample at four different times. All simultaions are carried out at a scan speed of 50 $\mu m/s$

13

To clarify the whole process from the beginning, the NP's SSD (solid green line), temperature (solid red line) and laser profiles (dashed blue line) are plotted in the same figures at various times (Figure 3(g) to (j)). The curves at different times clearly show the main stages during laser writing. At the first step, NPs inside the laser spot grow rapidly due to the positive feedback (Figure 3(g) and (h)). Accordingly, the temperature increases dramatically to 870 °C as illustrated in Figure 3(d) and (h)). After then, the shrinkage of NPs by oxidation dominates the process. The positive correlation between NPs size and absorption leads to the temperature decrease. As a matter of fact, the decreasing of temperature slows down the reaction speed, which in turn decreases the maximum size in the laser front edge (Figure 3(i)). The negative feedback continues until a steady state sets in. Afterward, the stationary stage persists till the end as plotted in Figure 3(i) to (j). Indeed, the above processes are valid for all scanning speeds that are lower than the maximum speed for NP growth. It is obvious that for high writing speeds that are comparable with the reaction rate, there is less time for NPs to grow. In this case, the laser-induced NP growth is not expected. The discussion will be presented in the next section.

Transforming the coupled equations into a moving coordinate system (MCS)[40] ($x = x' - \int_0^t V s(t')dt'$ and $t = t'$) implies the steady-state equations (see Eq. S1 in supplemental material). The stationary solutions depend on the moving boundary conditions that are hard to be calculated by FEM. The transient results of the extended 2D model reveal the existence of these kinds of solutions for various writing speeds (as shown in Figure 3 and Figure 4). To the best of our knowledge, stationary states are always observed in experiments, which is consistent with the theoretical prediction.

The photo-oxidation process is particularly important in the understanding of the speed-dependent final size. For all writing speeds, as discussed above, the NPs size profiles are nearly the same in the first stage owing to their rapid growth. In fact, the positive feedback stops as soon as the free Ag^0 atoms in matrix are exhausted as implied by Eq. 8. After size-shrinkage and temperature decrease, the stationary states are set with the total amount
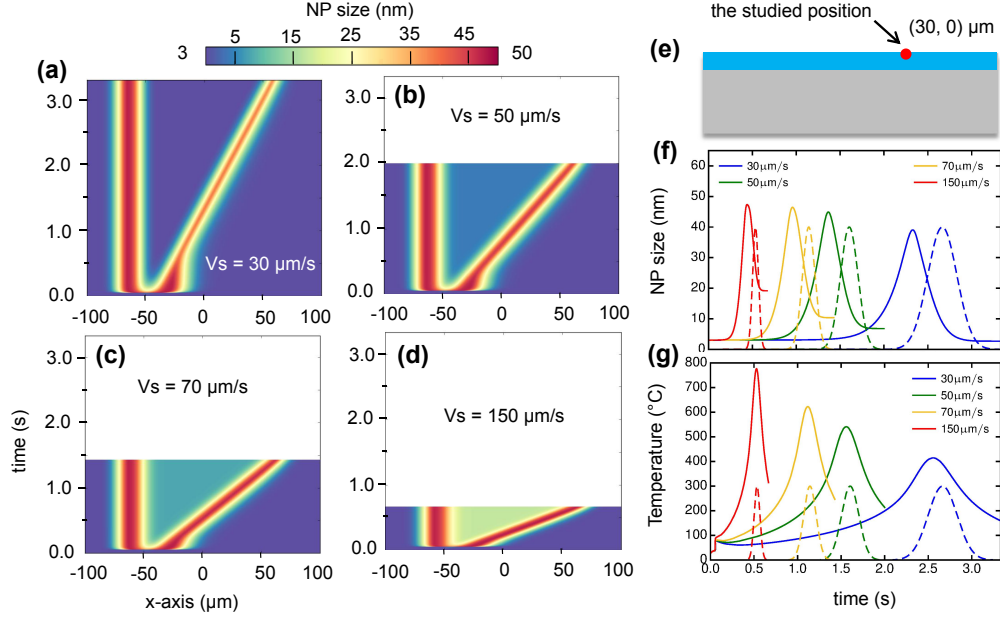
14

Figure 4: Time variation of the NP size along the translation direction at various writing speeds (a) to (d). To compare results at various speeds, the time variation of NP size (f) and temperature (g) at the studied position (e) are plotted. Dashed lines show when the laser beam reaches the studied location.

of photo-oxidized Ag^0 depending on the integration time of oxidation. In other words, there is more time at low scanning speeds to oxidize the NPs, so that lower temperatures are reached. The SSD width is broader at the beginning and thinner at stationary state as shown in Figure 4 (a) to (d). Note that reduction has little influence on the growth due to the low concentration of reducing agent, as reported by Liu et al.[12]

To get rid of the rapid growth at the beginning of the laser writing and to consider only the steady state behavior of the sample, the studied position is set at $x = 30\mu m$ (shown in Figure 4(e)) with its distance $80\mu m$ away from the laser center at $t = 0s$. Figure 4(f) plots the time vatiations of the NP size in this location for various writing speeds. The growth process lasts from a few tenths of a second to seconds, and the growth rate depends on the writing speed. According to Eq. 8, the temperature strongly affects the growth rate. This means that the sample experiences different temperatures at different speeds, which is clearly shown in Figure 4(g). In all cases, the growth is comparatively much slower than what was reported in reference.[12]

15

Heat diffusion is strongly contributes to the inhomogeneous SSD of NPs. According to Figure 4(f) and (g), for all writing speeds, NPs start to grow even before the laser arrives and the size increase is stopped before the maximum temperature is reached. It is clear that the heat diffusion due to phonon-phonon interaction is faster than the growth by atoms diffusion. Thus, the temperature has broader profiles than NP's SSD. That is why the NPs in the laser vicinity are pre-heated and once the temperature exceeds the activation threshold, NPs start growing up. Nevertheless, the temperature-dependent growth rate is faster than the studied writing speeds. Otherwise, the end of the growth process would be expected after reaching the maximum of temperature, or laser intensity.

Comparison with experiments

Experimentally, the transmissions are measured in the steady state far form the starting line. Herein, the discussion is then limited to the comparison with simulated results in steady-state. For each writing speed, we obtain the NPs' size profile after the laser moves $100\mu m$. The NP's SSDs are shown in Figure 5(a). Here, laser moves toward the positive x-axis with its intensity profile shown by the dashed black line. As discussed above, the maximum sizes appear before the laser-center arrives whatever the writing speed. To compare with the *in-situ* experiments, transmission profiles are retrieved based on two effective-medium models. The Maxwell-Garnett approximation is commonly used in literature.[41] However, it only valid for the NP sizes much smaller than laser wavelength.[36] For larger NPs, compared with MG, the Mie theory associated with Clausius-Mossotti equation[38] provides a size-dependent correction by accounting for the multipole contributions (CM-Mie).[36,37] The transmission profiles at wavelength 527 nm are calculated according to the Fresnel equation under normal incidence:

$$\text{Trans} = \frac{4Z_{air}Re(Z_{sub})}{|Z_{air}B + C|^2}$$

where

$$\begin{bmatrix} B \\ C \end{bmatrix} = \begin{bmatrix} cos\delta_m & jsin\delta_m/Z_m \\ jZ_m sin\delta_m & cos\delta_m \end{bmatrix} \begin{bmatrix} 1 \\ Z_{sub} \end{bmatrix} \qquad (17)$$

$$\delta_m = 2\pi n_m h_f/\lambda$$

where Z_i is the media impedance (i = air, effective medium or glass substrate), $h_f = 200nm$ the film thickness, and n_m the effective index.
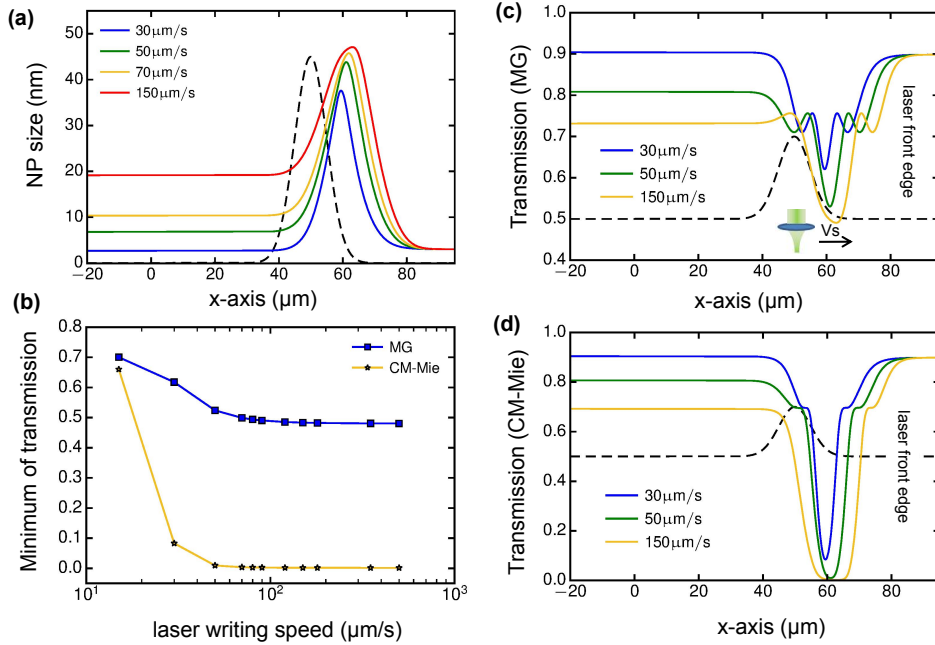

Figure 5: Simulated NP size and transmission along the writing line at the end of the calculation for various writing speeds. NP size (a). Sample transmission calculated by Maxwell-Garnett (c) or Mie coupled with Clausius-Mossotti model (d). Minimum transmission versus writing speed for the two models (b). The dashed lines stand for the laser profiles.

Figure 5(c) and (d) show the retrieved transmission profiles at various writing speeds based on MG and CM-Mie respectively. Though the value of transmission by MG and CM-Mie differ, the trends are quite similar: the transmission decreases in the laser front edge before growing back inside the irradiated area. No matter which EM model is used, the position at transmission minimum is always located at the laser front edge for every

writing speed. The calculations show that the transmission minimum is close to the location of the largest NPs in laser front edge. Furthermore, the transmission minimum decreases and saturates while increasing the writing speed. These works are consistent with the in-situ experiments (Figure 1). The mechanisms behind have been discussed in the previous section.

Activation energy of diffusion

The activation energy of metal ion diffusion in the studied system affects NP's growth threshold. The exact activation energy in the mesoporous TiO_2 film is not known to the best of our knowledge. As a rule of thumb, the activation energy is estimated from the Ag diffusion in silicon dioxide and copper, which gives the value around 1.0eV.[12,27,28] Thus, a reasonable value for Ag in mesoporous TiO_2 ranges from 0.5eV to 1.5eV.[12]
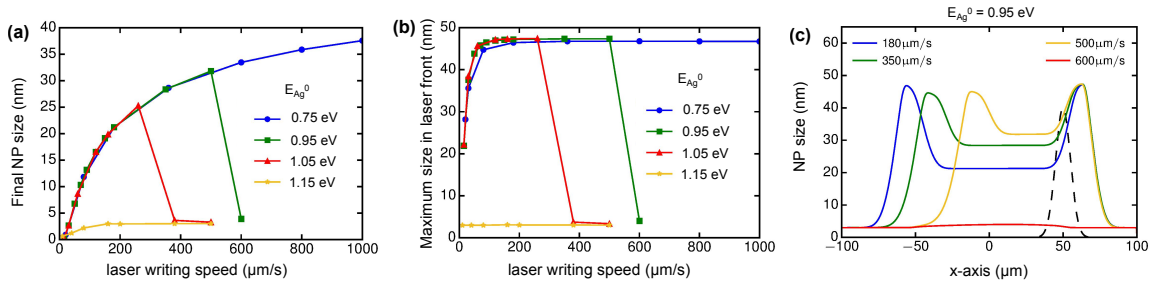

Figure 6: Influences of the activation energy of free Ag^0 diffusion ($\eta_0 = 2.3 \times 10^{-5}$). The final NP size after laser scanning (a) and the maximum size in the laser front (b) for various activation energy, and (c) the spatial distribution of NP size with $E_{Ag^0} = 0.95$eV.

To understand how the activation energy influences the NP growth, the NP final size and maximum size in the laser front edge are calculated at various scanning speeds with different activation energies. They are shown in Figure 6(a) and (b). Interestingly, the maximum size never exceeds 4 nm for activation energy $E_{Ag^0} = 1.15$eV. In this case, the activation energy is too high to allow the rapid positive feedback to appear. The size increase and saturation occur for lower energies. Moreover, the activation energy never alters the final size and maximum size profiles except for the high writing speeds. It means that the activation energy has a little impact on the saturation process. Instead, an increase of the activation energy decreases the growing speed that has a great influence on the up-threshold of writing

18

speed. To understand what happens at high speed, NP size profiles are plotted in Figure 6(c) at various scanning speeds along x-axis. At high speed the growth never starts since there is not enough time for NPs in a rapid moving laser spot (e.g. $600\mu m/s$) to grow large enough to activate the feedback promptly.
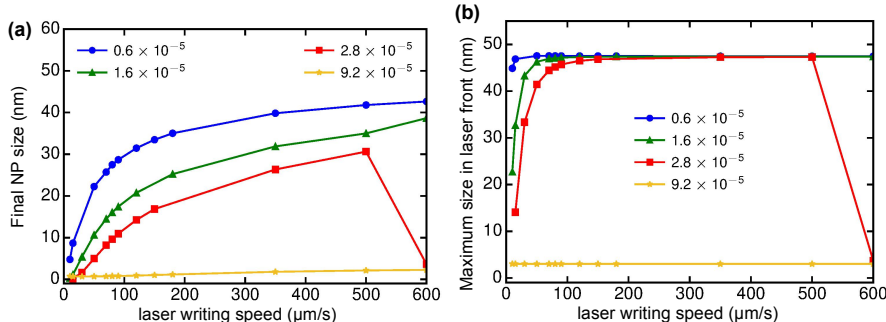

Figure 7: Influence of ionization efficiency ($E_{Ag^0} = 0.95$eV). Final NP size after laser writing (a) and Maximum size in the laser front edge (b).

Oxidation rates

The photo-oxidation process strongly affects the steady-state parameters. Figure 7 shows the dependence of the NP final size and maximum size on the writing speed at various oxidation rates. The two size-profiles saturate at lower speeds while decreasing the oxidation rate. The result again confirms the fact that the oxidation process contributes greatly to the scanning speed dependent phenomenon. Once the rapid feedback is activated, the fast growth of NPs never stops until the concentration of Ag^0 decreases to the value close to Ag^0 solubility. This is also the reason why the activation energy (E_{Ag^0}) never alters the saturation profile. On the contrary, the oxidation leads to the size-shrinkage with an amount inversely proportional to the scanning speed. The suggested NP size increases while decreasing the oxidation rate for the same scanning speed. Owing to the positive correlation between absorption and size, lower oxidation rates saturate at lower speeds. Furthermore, oxidation affects the positive feedback. For a given activation energy, an increase of the oxidation rate means more time is required for a NP to grow above a threshold size. This is the case for oxidation rate

19

$\eta_0 = 1.6 \times 10^{-5}$ and $\eta_0 = 2.8 \times 10^{-5}$ at 600μm/s. For the high oxidation rate $\eta_0 = 9.2 \times 10^{-5}$ as shown in Figure 7, the rapid positive feedback never appears.

Conclusions

We have performed *in-situ* experiments and observed the inhomogeneous transmission along the laser writing lines. To understand the underlying phenomena, we have proposed an extended and self-consistent model of laser-induced Ag NP growth in TiO$_2$ film. The multi-scale problem has been theoretically investigated by introducing the Bulirsch-Stoer algorithm coupled with Finite Element Method, so that the extended 2D model was solved numerically in an affordable time. The extended 2D model takes into consideration spatial size-distribution of NPs and provides new insights into the understanding of the writing speed-dependent phenomena.

Firstly, the silver NPs have been shown to grow in the laser front edge due to pre-heating by thermal diffusion. Secondly, photo-oxidation has been found to be responsible for the writing speed-dependent size. The spatial size-distribution and temperature profile vary dynamically until a steady-state appears. The implied stationary solutions of the Moving coordinate system are found to exist for various speeds by the transient analyses.

Furthermore, the activation energy of Ag^0 diffusion has been shown to affect the growing speed, but to only slightly influence the size-saturation. On the contrary, the ionization efficiency is found to have a great impact on the saturation, which again proves the important role of oxidation in the speed controlled phenomena. In the meantime, high oxidation prohibits the rapid growth of NPs that levels up the threshold size of the positive feedback.

The proposed study provides an overview of the influences of Ag^0 activation energy and ionization efficiency in mesoporous TiO$_2$ film on the NP size, which gives a new route for comparing the ionization efficiency in different samples.

We note, finally, that the proposed model can be also applied for many similar sys-

tems composed of metallic nanoparticles embedded in semiconductors such as, for instance, Ag:ZnO or Au:TiO$_2$.

Acknowledgement

Supporting Information Available

Table of simulating parameters, steady-state equations in a moving coordinate system, permittivity by CM-Mie and MG theory, and transmission along the laser writted line center at high scanning speeds. This material is available free of charge via Internet at http://pubs.acs.org.

References

(1) Atwater, H. A.; Polman, A. Plasmonics for improved photovoltaic devices. *Nat. Mater.* **2010**, *9*, 205.

(2) Nakayama, K.; Tanabe, K.; Atwater, H. A. Plasmonic nanoparticle enhanced light absorption in GaAs solar cells. *Appl. Phys. Lett.* **2008**, *93*, 121904.

(3) Kawata, S.; Inouye, Y.; Verma, P. Plasmonics for near-field nano-imaging and super-lensing. *Nat. Photonics* **2009**, *3*, 388.

(4) Anker, J.; Hall, W.; Lyandres, O.; Shah, N.; Zhao, J.; Van Duyne, R. Biosensing with plasmonic nanosensors. *Nat. Mater.* **2008**, *7*, 442–453.

(5) Brongersma, M. L.; Halas, N. J.; Nordlander, P. Plasmon-induced hot carrier science and technology. *Nat. Nanotechnol.* **2015**, *10*, 25.

(6) Clavero, C. Plasmon-induced hot-electron generation at nanoparticle/metal-oxide interfaces for photovoltaic and photocatalytic devices. *Nat. Photonics* **2014**, *8*, 95.

(7) Yin, X.; Ye, Z.; Rho, J.; Wang, Y.; Zhang, X. Photonic spin Hall effect at metasurfaces. *Science* **2013**, *339*, 1405–1407.

(8) Luk'yanchuk, B.; Zheludev, N. I.; Maier, S. A.; Halas, N. J.; Nordlander, P.; Giessen, H.; Chong, C. T. The Fano resonance in plasmonic nanostructures and metamaterials. *Nat. Mater.* **2010**, *9*, 707.

(9) Ergin, T.; Stenger, N.; Brenner, P.; Pendry, J. B.; Wegener, M. Three-dimensional invisibility cloak at optical wavelengths. *Science* **2010**, 1186351.

(10) Matsumoto, Y.; Murakami, M.; Shono, T.; Hasegawa, T.; Fukumura, T.; Kawasaki, M.; Ahmet, P.; Chikyow, T.; Koshihara, S.-y.; Koinuma, H. Room-temperature ferromagnetism in transparent transition metal-doped titanium dioxide. *Science* **2001**, *291*, 854–856.

(11) Naoi, K.; Ohko, Y.; Tatsuma, T. TiO2 films loaded with silver nanoparticles: control of multicolor photochromic behavior. *J. Am. Chem. Soc.* **2004**, *126*, 3664–3668.

(12) Liu, Z.; Destouches, N.; Vitrant, G.; Lefkir, Y.; Epicier, T.; Vocanson, F.; Bakhti, S.; Fang, Y.; Bandyopadhyay, B.; Ahmed, M. Understanding the growth mechanisms of Ag nanoparticles controlled by plasmon-induced charge transfers in Ag-TiO2 films. *J. Phys. Chem. C* **2015**, *119*, 9496–9505.

(13) Baraldi, G.; Bakhti, S.; Liu, Z.; Reynaud, S.; Lefkir, Y.; Vocanson, F.; Destouches, N. Polarization-driven self-organization of silver nanoparticles in 1D and 2D subwavelength gratings for plasmonic photocatalysis. *Nanotechnology* **2016**, *28*, 035302.

(14) Liu, Z.; Siegel, J.; Garcia-Lechuga, M.; Epicier, T.; Lefkir, Y.; Reynaud, S.; Bugnet, M.; Vocanson, F.; Solis, J.; Vitrant, G. et al. Three-dimensional self-organization in nanocomposite layered systems by ultrafast laser pulses. *ACS Nano* **2017**, *11*, 5031–5040.

(15) Arndt, D.; Bangerth, W.; Davydov, D.; Heister, T.; Heltai, L.; Kronbichler, M.; Maier, M.; Pelteret, J.-P.; Turcksin, B.; Wells, D. The deal. II library, version 8.5. *J. Numer. Math.* **2017**, *25*, 137–145.

(16) Crespo-Monteiro, N.; Destouches, N.; Epicier, T.; Balan, L.; Vocanson, F.; Lefkir, Y.; Michalon, J.-Y. Changes in the chemical and structural properties of nanocomposite Ag: TiO2 films during photochromic transitions. *J. Phys. Chem. C* **2014**, *118*, 24055–24061.

(17) Liu, Z.; Epicier, T.; Lefkir, Y.; Vitrant, G.; Destouches, N. HAADF-STEM characterization and simulation of nanoparticle distributions in an inhomogeneous matrix. *Journal of microscopy* **2017**, *266*, 60–68.

(18) Crespo-Monteiro, N.; Destouches, N.; Bois, L.; Chassagneux, F.; Reynaud, S.; Fournel, T. Reversible and irreversible laser microinscription on silver-containing mesoporous titania films. *Adv. Mater.* **2010**, *22*, 3166–3170.

(19) Crespo-Monteiro, N.; Destouches, N.; Saviot, L.; Reynaud, S.; Epicier, T.; Gamet, E.; Bois, L.; Boukenter, A. One-step microstructuring of TiO2 and Ag-TiO2 films by continuous wave laser processing in the UV and visible ranges. *J. Phys. Chem. C* **2012**, *116*, 26857–26864.

(20) Babonneau, D.; Diop, D.; Simonot, L.; Lamongie, B.; Blanc, N.; Boudet, N.; Vocanson, F.; Destouches, N. Real-time investigations of structural and optical changes in photochromic Ag/TiO2 nanocomposite thin films under laser irradiation. *Nano Futures* **2018**, *2*, 015002.

(21) Crespo-Monteiro, N.; Destouches, N.; Nadar, L.; Reynaud, S.; Vocanson, F.; Michalon, J. Irradiance influence on the multicolor photochromism of mesoporous TiO2 films loaded with silver nanoparticles. *Appl. Phys. Lett.* **2011**, *99*, 173106.

(22) Kazuma, E.; Sakai, N.; Tatsuma, T. Nanoimaging of localized plasmon-induced charge separation. *Chem. Commun.* **2011**, *47*, 5777–5779.

(23) Kazuma, E.; Tatsuma, T. Photoelectrochemical analysis of allowed and forbidden multipole plasmon modes of polydisperse Ag nanorods. *J. Phys. Chem. C* **2012**, *117*, 2435–2441.

(24) Kawahara, K.; Suzuki, K.; Ohko, Y.; Tatsuma, T. Electron transport in silver-semiconductor nanocomposite films exhibiting multicolor photochromism. *Phys. Chem. Chem. Phys.* **2005**, *7*, 3851–3855.

(25) Kaganovskii, Y.; Lipovskii, A.; Rosenbluh, M.; Zhurikhina, V. Formation of nanoclusters through silver reduction in glasses: the model. *J. Non-Cryst. Solids* **2007**, *353*, 2263–2271.

(26) Liu, Z.; Vitrant, G.; Lefkir, Y.; Bakhti, S.; Destouches, N. Laser induced mechanisms controlling the size distribution of metallic nanoparticles. *Phys. Chem. Chem. Phys.* **2016**, *18*, 24600–24609.

(27) McBrayer, J. D.; Swanson, R.; Sigmon, T. Diffusion of metals in silicon dioxide. *J. Electrochem. Soc.* **1986**, *133*, 1242–1246.

(28) Butrymowicz, D. B.; Manning, J. R.; Read, M. E. Diffusion in Copper and Copper Alloys, Part II. Copper-Silver and Copper-Gold Systems. *J. Phys. Chem. Ref. Data* **1974**, *3*, 527–602.

(29) Landau, L. D.; Lifshitz, E.; Pitaevskij, L. *Course of theoretical physics. vol. 10: Physical kinetics*; Oxford, 1981; pp 431–433.

(30) Thanh, N. T.; Maclean, N.; Mahiddine, S. Mechanisms of nucleation and growth of nanoparticles in solution. *Chem. Rev.* **2014**, *114*, 7610–7630.

(31) Kwon, S. G.; Hyeon, T. Formation mechanisms of uniform nanocrystals via hot-injection and heat-up methods. *Small* **2011**, *7*, 2685–2702.

(32) Delfour, L.; Itina, T. E. Mechanisms of ultrashort laser-induced fragmentation of metal nanoparticles in liquids: numerical insights. *J. Phys. Chem. C* **2015**, *119*, 13893–13900.

(33) Metwally, K.; Mensah, S.; Baffou, G. Fluence threshold for photothermal bubble generation using plasmonic nanoparticles. *J. Phys. Chem. C* **2015**, *119*, 28586–28596.

(34) Pustovalov, V. K. Light-to-heat conversion and heating of single nanoparticles, their assemblies, and the surrounding medium under laser pulses. *RSC Adv.* **2016**, *6*, 81266–81289.

(35) Plech, A.; Kotaidis, V.; Grésillon, S.; Dahmen, C.; Von Plessen, G. Laser-induced heating and melting of gold nanoparticles studied by time-resolved X-ray scattering. *Phys. Rev. B: Condens. Matter* **2004**, *70*, 195423.

(36) Malasi, A.; Kalyanaraman, R.; Garcia, H. From Mie to Fresnel through effective medium approximation with multipole contributions. *J. Opt.* **2014**, *16*, 065001.

(37) Doyle, W. T. Optical properties of a suspension of metal spheres. *Phys. Rev. B: Condens. Matter* **1989**, *39*, 9852.

(38) Rysselberghe, P. V. Remarks concerning the Clausius-Mossotti law. *The Journal of Physical Chemistry* **1932**, *36*, 1152–1155.

(39) Press, W.; Teukolsky, S.; Vetterling, W.; Flannery, B. Section 17.3 Richardson Extrapolation and the Bulirsch-Stoer Method. *Numerical Recipes: The Art of Scientific Computing, Cambridge University Press, New York, NY* **2007**,

(40) Jensen, O. K.; Finlayson, B. A. Solution of the transport equations using a moving coordinate system. *Adv. Water Resour.* **1980**, *3*, 9–18.

(41) Pedrueza, E.; Valdés, J. L.; Chirvony, V.; Abargues, R.; Hernández-Saz, J.; Herrera, M.; Molina, S. I.; Martínez-Pastor, J. P. Novel method of preparation of gold-nanoparticle-doped TiO2 and SiO2 plasmonic thin films: optical characterization and comparison with Maxwell–Garnett modeling. *Adv. Funct. Mater.* **2011**, *21*, 3502–3507.

Graphical TOC Entry